

Article

Slot-Waveguide Based All-Optical RF Spectrum Analyzer

Yuhua Li ¹, Zhe Kang ² , Wai-Lok Ho ³, Roy R. Davidson ⁴, Brent E. Little ⁴, Sai-Tak Chu ³ and Kun Zhu ^{5,*} 

¹ Key Laboratory of Optical Field Manipulation of Zhejiang Province, Department of Physics, Zhejiang Sci-Tech University, Hangzhou 310018, China

² Center for Optical and Electromagnetic Research, College of Optical Science and Engineering, National Engineering Research Center for Optical Instruments, Ningbo Innovation Center, Zhejiang University, Hangzhou 310058, China

³ Department of Physics, City University of Hong Kong, Kowloon, Hong Kong SAR 999077, China

⁴ QXP Technologies Inc., Xi'an 710311, China

⁵ Photonics Research Institute, Department of Electrical and Electronic Engineering, The Hong Kong Polytechnic University, Kowloon, Hong Kong SAR 999077, China

* Correspondence: kun.zhu@polyu.edu.hk

Abstract: All-optical radio-frequency spectrum analyzers (AORFSAs) with ultrabroad bandwidth break the electronic bottleneck and provide an efficient frequency analysis means for ultrafast optical signals in communications, signal generation and processing systems. Here, we propose and experimentally demonstrate an AORFSA built on the cross-phase modulation effect in a 50 cm long CMOS-compatible photonic slot-waveguide. The waveguide has a 100 nm thick thin-film core of fused silica that is sandwiched by two 750 nm thick cladding layers of high-index doped silica, which shows optimized dispersion and comparable nonlinear characteristics. The measured 3 dB bandwidth of the proposed slot-waveguide-based AORFSA has a three-fold increase over the conventional channel waveguide having the same dimension and length. The sensitivity and wavelength- and polarization-dependence properties are investigated, confirming the proposed waveguide as a versatile platform for frequency analysis of ultrafast optical signals, such as Kerr microcombs with hundreds of GHz or even THz mode spacing.

Keywords: nonlinear optics; optical signal processing; slot-waveguides; radio-frequency (RF) spectrum analysis



Citation: Li, Y.; Kang, Z.; Ho, W.-L.; Davidson, R.R.; Little, B.E.; Chu, S.-T.; Zhu, K. Slot-Waveguide Based All-Optical RF Spectrum Analyzer. *Photonics* **2023**, *10*, 1380. <https://doi.org/10.3390/photonics10121380>

Received: 2 November 2023

Revised: 10 December 2023

Accepted: 12 December 2023

Published: 15 December 2023



Copyright: © 2023 by the authors. Licensee MDPI, Basel, Switzerland. This article is an open access article distributed under the terms and conditions of the Creative Commons Attribution (CC BY) license (<https://creativecommons.org/licenses/by/4.0/>).

1. Introduction

With the rapid development of ultrahigh-speed optical telecommunication and signal processing systems nowadays, there has been great demand for measuring and analyzing ultrafast signals with their spectrum diagnostics, especially in the fields of optical signal impairment monitoring in optical communication systems [1–3], full characterization of ultrafast optical pulse sources [4,5], microwave photonics [6,7], etc. The radio-frequency (RF) spectrum of an optical signal is the power spectrum of its temporal intensity, i.e., the power spectral density of its autocorrelation. The conventional approach to measuring it is first using an ultrafast photodetector to capture the temporal envelope and then resolving the spectrum with an electrical spectrum analyzer. Such a method is invalid in applications with the need to measure optical signals with a frequency beyond 100 GHz due to the inherent limitation of response bandwidth in current optical-to-electrical (O/E) conversion and electronic components [6].

The nonlinear Kerr effect provides a passive method to directly measure the RF spectrum of an optical signal in the optical domain with a remarkably large bandwidth and without any O/E conversion. Built on the ultrafast cross-phase modulation (XPM) effect, the RF spectrum of the signal beam under test is mapped to the optical spectrum of the probe beam, with which the electronic bandwidth limitation beyond 100 GHz can be easily overcome [8–10]. The first all-optical RF spectrum analyzer (AORFSA) was demonstrated

by C. Dorrer and D. N. Maywar using highly nonlinear fiber (HNLF), which achieved a bandwidth of analysis up to 800 GHz [11]. To reduce the footprint, instead of using bulky optical fibers, various passive nonlinear photonic-integration waveguide platforms of different materials have been introduced for the AORFSAs, such as silicon [12–14], chalcogenide [3,8,15], high-index doped silica [16,17] and silicon nitride [18]. For the high-index doped silica glass waveguide AORFSA, the first demonstration was in 2014 on a ~4 cm long waveguide exhibited a bandwidth of 2.5 THz [16]. The AORFSA bandwidth was further improved to 5 THz on a 50 cm long waveguide that had its dimension adjusted for dispersion engineering [17]. Besides changing the waveguide dimension, it is also possible to engineer the waveguide dispersion by embedding a slot in the middle of the waveguide [19,20]. The effectiveness of the slot structure in engineering the dispersion profile of silicon-rich waveguides has been demonstrated in previous studies [21–23]. When a slot is added, it transforms the traditional channel waveguide into a coupled structure that supports both symmetric and asymmetric supermodes [24,25]. The symmetric mode, which is present in both polarizations, exhibits a concave dispersion profile, making it useful for flattening the convex shape of the dispersion profile of the channel waveguide. Notably, the TM mode with the optical field perpendicular to the slot interfaces has a more pronounced dispersion-flattening effect due to the enhanced intensity at the slot interfaces. In this work, we would like to investigate the effectiveness of using the slot-waveguide in the AORFSA application by comparing the AORFSA performances between the slot-waveguide and the regular channel waveguide.

The slot-waveguide considered in this work consists of a high-index doped silica glass core with a thin SiO₂ slot layer embedded in the center. The waveguide dispersion is optimized with the zero-dispersion location lying within the C and L bands to ease the group velocity “walk-off” and to increase the AORFSA working bandwidth. Note that the proposed method can also be applied to other wavelength bands, since the inherent principle behind AORFSA is wavelength-independent. We chose the C and L bands in this work because these telecom sources are widely available and are well developed for ultrafast optics. In applications such as mode-locked lasers and femtosecond fiber lasers, it is important to characterize these ultrafast signals in the RF domain. However, the RF bandwidths of these signals can often go beyond 100 GHz, and we have to adopt other schemes such as the AORFSA instead of using the traditional electronic spectrum analyzer with limited bandwidth. The addition of the slot only impacted the $\chi^{(3)}$ nonlinearity and propagation loss slightly, which were comparable to those of the high-index doped silica channel waveguides, where the nonlinear loss from the two-photon absorption (TPA) effect is also negligible in the telecom bands [16,26]. The waveguide is fully CMOS-compatible, which makes it possible for on-chip dense manufacturing and integration with other optical components. The measured 3 dB bandwidth of the proposed slot-waveguide-based AORFSA has a three-fold increase over the conventional channel waveguide. The performance of the AORFSA, such as its sensitivity and wavelength- and polarization-dependence properties, is investigated and compared with that of the channel waveguide in the following sections.

2. Methods

The RF spectrum $S_S(\omega)$ of the optical signal under test (SUT) is the power spectrum of the intensity $I(t)$ of the temporal waveform, and its optical spectrum $O_S(\omega)$ is the power spectrum of the electric field $E(t)$ [11], as given by

$$S_S(\omega) = \left| \int I(t) \exp(i\omega t) dt \right|^2. \quad (1)$$

$$O_S(\omega) = \left| \int E(t) \exp(i\omega t) dt \right|^2. \quad (2)$$

The principal diagram of the AORFSA is shown in Figure 1. The optical signal under test and a monochromatic CW probe light beam are coupled and co-propagate through a nonlinear medium, e.g., HNLF or a nonlinear waveguide. Due to the XPM effect, the phase of the CW probe beam is modulated by the varied intensity of the SUT. Assuming the electric field of the input CW probe light is $E_p(t) = E_0 \exp(-i\omega_p t)$, the electric field output from the nonlinear medium is given by

$$E'_p(t) = E_0 \exp(-i\omega_p t) \exp[mI(t)], \tag{3}$$

where ω_p is the probe frequency, $I(t)$ is the temporal intensity of the SUT and m is a complex index that equals $(i \cdot 4\pi \cdot n_2 / \lambda_S \cdot A_{eff} - \beta_T / 2A_{eff}) \cdot L$, with n_2 being the nonlinear refractive index, λ_S the averaged wavelength of the SUT and β_T the TPA parameter. In our scenario, the TPA term equals zero since the proposed slot-waveguide does not suffer the TPA effect. A_{eff} represents the effective mode area of the waveguide. Since the modulation from XPM is a small term, the output electric field can be written using Taylor expansion as follows:

$$E'_p(t) = E_0 \exp(-i\omega_p t) \cdot [1 + mI(t)]. \tag{4}$$

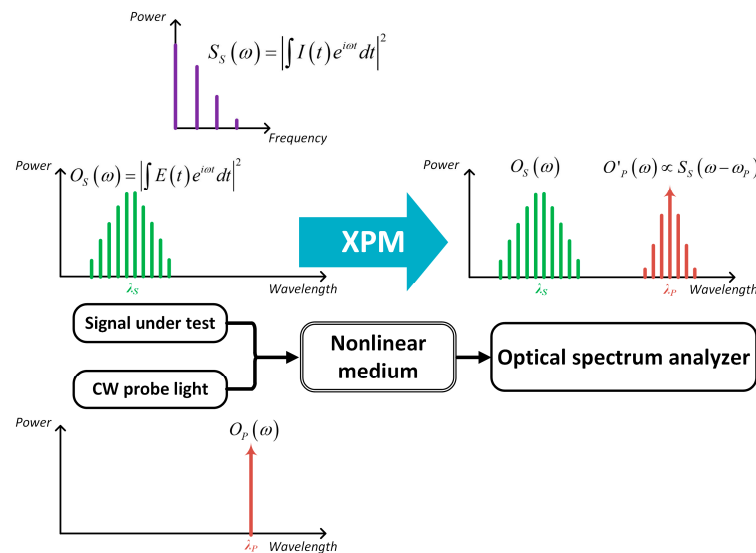


Figure 1. Principle diagram of the all-optical RF spectrum analyzer. Through the XPM effect between the optical SUT and the CW probe light, the RF spectrum of the SUT $S_S(\omega)$ is mapped to the optical spectrum of the probe light $O'_p(\omega)$.

After the Fourier transform, the optical spectrum of the modulated probe light is given by

$$O'_p(\omega) = \left| \int E'_p(t) \exp(i\omega t) dt \right|^2 = \left| E_0 \int [1 + mI(t)] \exp(i(\omega - \omega_p)t) dt \right|^2 = E_0^2 \delta(\omega - \omega_p) + E_0^2 |m|^2 S_S(\omega - \omega_p). \tag{5}$$

We note that the optical spectrum of the output probe light consists of two parts. The first term is a Dirac delta function centered at ω_p that indicates the original spectrum of the input CW probe beam, while the second term is proportional to the RF spectrum of the SUT around ω_p with a factor of $E_0^2 |m|^2$. Thus, the RF spectrum of the SUT can be obtained as

$$O'_p(\omega) \propto \left(E_0 \cdot n_2 \cdot L / (\lambda_S \cdot A_{eff}) \right)^2 S_S(\omega - \omega_p) \propto (E_0 L \gamma)^2 S_S(\omega - \omega_p), \tag{6}$$

where γ is the nonlinear coefficient of the waveguide that equals $2\pi \cdot n_2 / (\lambda_S \cdot A_{eff})$. This means the RF spectrum of the SUT can be obtained by directly measuring the optical spectrum of the output probe light centered at ω_p with an optical spectrum analyzer (OSA),

as shown in Figure 1. We note that the residual spectrum of the CW beam centered at ω_p should be filtered out during the AORFSA process. The RF spectrum of the SUT is mapped to the optical spectrum of the probe beam in both upper and lower bands.

3. Experiment

The proposed slot-waveguide for the AORFSA application was fabricated using a CMOS-compatible high-index glass waveguide fabrication process [27]. The scanning electron microscope (SEM) image of the cross-section of the core of the fabricated slot-waveguide is shown in Figure 2a, which has a thin 100 nm slot layer composed of PECVD oxide with $n = 1.445$ that is sandwiched by two 750 nm thick high-index doped silica layers with $n = 1.70$. The width of the waveguide is $\sim 4 \mu\text{m}$, with a slight sidewall angle of ~ 4 degrees. Figure 2b shows the photo from the top of the 50 cm long spiral waveguide, which is integrated into a chip of $1 \text{ cm} \times 1 \text{ cm}$, which can greatly decrease the footprint of the whole chip. The waveguide was attached to the fiber pigtailed through the on-chip edge coupler, with the coupling loss between the optical fiber and the waveguide being $\sim 1 \text{ dB/facet}$. Figure 2c–f show the simulated profiles of the electric field distribution of both the TE and TM modes. It can be seen from Figure 2e,f that for the TM mode, the electric field is squeezed into the slot region due to the large electric field discontinuity at the interface with high-index contrast [28,29].

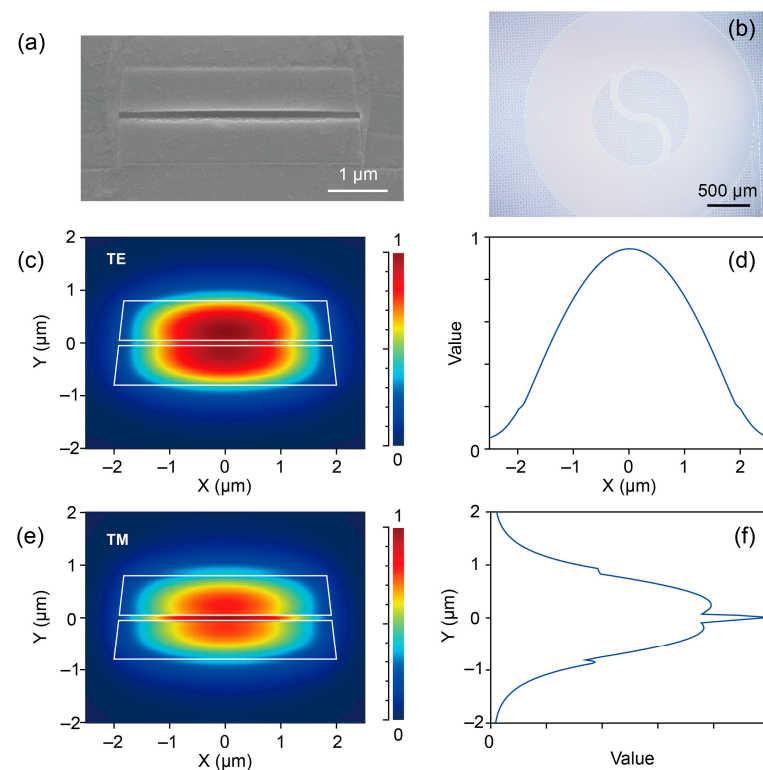


Figure 2. (a) SEM image of the cross-section of the fabricated slot-waveguide. (b) Overall image of the fabricated 50 cm long spiral slot-waveguide. (c,d) The simulated electric field profile and its corresponding amplitude along the X direction at $y = 0$ for the TE mode. (e,f) The simulated electric field profile and its corresponding amplitude along the Y direction at $x = 0$ for the TM mode.

Figure 3 shows the simulated dispersion characteristics of both the conventional channel waveguide and the proposed slot-waveguide with the same dimension. The zero-dispersion wavelengths for the TM and TE modes of the slot-waveguide are 1580 nm and 1600 nm, respectively. Compared with the relatively large dispersion of the channel waveguide, the dispersion of the slot-waveguide is within $30 \text{ ps}/(\text{nm}\cdot\text{km})$ for the TE mode and within $20 \text{ ps}/(\text{nm}\cdot\text{km})$ for the TM mode in the whole C and L bands. This indicates

that the geometry of the slot-waveguide is well designed to tailor the dispersion. With less accumulated dispersion in the operating band, the group velocity “walk-off” issue can be mitigated, which permits a larger measuring bandwidth. The propagation loss of the 50 cm long spiral slot-waveguide is measured by the cutback method. For the TE polarization, the propagation loss is below 0.10 dB/cm between 1550 nm and 1610 nm, and the amount for the TM polarization is below 0.11 dB/cm. As shown in Table 1, the propagation loss only increases slightly for the slot structure. The nonlinearity γ is measured by the four-wave-mixing (FWM) method [30], the values of which for both the slot and channel waveguides are included in Table 1. The same order of magnitude of nonlinearity can be observed with the two waveguides for both the TE and TM modes. Although the nonlinear refractive index n_2 of silica is one order of magnitude smaller than that of the high-index doped silica, the effective area A_{eff} of the slot-waveguide is reduced by squeezing the electric field into the silica slot core. Thus, the large nonlinearity is almost preserved compared with the channel structure. In general, by inserting a slot core layer, we optimize the dispersion of the waveguide without sacrificing its loss and nonlinearity. This means that, in the application of AORFSA, the proposed slot-waveguide can achieve a larger measuring bandwidth with the same sensitivity level, or we can use a longer nonlinear waveguide to increase its sensitivity and signal-to-noise ratio (SNR) for a given measurement bandwidth.

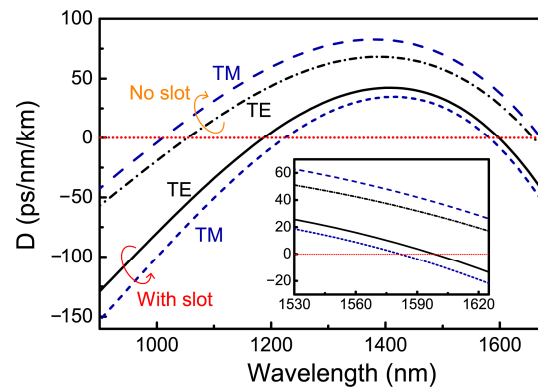


Figure 3. The calculated dispersion of the fabricated standard channel waveguide and the slot-waveguide for both TE and TM modes. Inset: the dispersion characteristic in the C and L bands.

Table 1. Measured and simulated characteristics of the slot-waveguide and the conventional channel waveguide.

Waveguide/Mode	Dispersion @1555 nm (ps/nm/km)	Dispersion Slope @1550 nm (ps/nm ² /km)	Propagation Loss @1550 nm (dB/cm)	γ (/W/km)
With slot/TM	10.5	−0.42	0.11	190
With slot/TE	17.7	−0.42	0.10	130
No slot/TM	55.1	−0.39	0.09	180
No slot/TE	44.0	−0.36	0.07	100

4. Experimental Results and Discussion

4.1. Bandwidth

As one of the key parameters, the measurement bandwidth of the AORFSA is determined by both the response time of nonlinear interaction and the phase matching effect, i.e., the group velocity “walk-off” issue [11]. Since the response time of the Kerr effect is as fast as the femtosecond level, the bandwidth of the AORFSA is mostly affected by the group velocity mismatch, which degrades the efficiency of the XPM process. Considering the group velocity mismatch effect [11], the RF spectrum of the SUT is given by

$$O'_p(\omega) \propto (E_0 L \gamma)^2 \cdot S_S(\omega - \omega_p) \cdot \sin^2 \left(\frac{L}{2} \cdot \left(\frac{1}{v_S} - \frac{1}{v_P} \right) \cdot (\omega - \omega_p) \right), \quad (7)$$

where v_S and v_P are the group velocities of the SUT and the monochromatic CW probe beam, respectively. The bandwidth of the AORFSA can then be estimated as

$$\Delta f_{\max} = \frac{1}{L \left| 2D\Delta\lambda + \frac{\partial D}{\partial \lambda} \Big|_{\lambda_S} \cdot \Delta\lambda^2 \right|}, \tag{8}$$

where D is the dispersion parameter, $\partial D/\partial \lambda$ is the dispersion slope around the SUT wavelength λ_S and $\Delta\lambda$ is the wavelength detuning between the SUT and the CW probe beam [16]. It should be mentioned that self-phase modulation (SPM) may distort the spectrum measurement at higher power levels. But in our case, the lower dispersion feature of the slot-waveguide can prevent this signal distortion, allowing for a larger input power to make the AORFSA have a larger dynamic range in the measurement. The influence of the probe beam itself on the measurement results can be negligible. Firstly, it is easy to find an optical source with stable power output as the probe beam. Secondly, the bandwidth or linewidth of the probe beam is always much smaller than the SUT's bandwidth (normally over 100 GHz). So, normally, we do not need to consider the influence of the probe beam itself.

The bandwidth measurement of the AORFSA is normally performed by monitoring the RF spectrum of an optical signal of two wavelengths (i.e., with a single-frequency response) [11]. To measure the frequency response of the AORFSA, two tunable laser sources (TLs1 and TLs2) whose wavelengths are adjusted between 1550 nm and 1565 nm with the frequency spacing changing from 0 to 1.88 THz are used as the SUT. TLs3, with a wavelength fixed at 1580 nm, acts as the CW probe beam. Erbium-doped fiber amplifiers are used to compensate for the link loss, followed by optical bandpass filters for removing the amplified stimulated emission (ASE) noise. The output optical signals from the slot-waveguide are analyzed with an OSA (Yokogawa, AQ6370D).

Figure 4a shows the output optical spectrum when λ_1 , λ_2 and λ_3 are located at 1550 nm, 1558 nm and 1580 nm, respectively. Two XPM signals are generated around the probe beam λ_3 with a spacing of 8 nm that is equal to the wavelength spacing between λ_1 and λ_2 . Different FWM signals are also found in Figure 4a. We notice that the FWM signals between the probe and SUT cannot fall into the band for the measurement [11]. The spectral overlap between the FWM signals and the probe is detrimental to the bandwidth. Both $FWM_{S,P}$ and $FWM_{S,S}$ can distort the measured RF spectrum if they go into the upper or lower band of the probe, as shown in Figure 4a. In most cases, $FWM_{S,S}$ is larger than $FWM_{S,P}$ since we can put the wavelength of the probe far away from the SUT to decrease $FWM_{S,P}$. In this way, we can also prevent $FWM_{S,S}$ from falling into the measuring band of the probe. In our scenario, if the upper band shown in Figure 4a is used for measuring the RF spectrum, the sweep wavelength λ_2 cannot be made larger than $(\lambda_1 + \lambda_3)/2$ to ensure that the FWM between λ_2 and λ_3 is out of the upper measuring band. As a result, Figure 4b shows the normalized optical power of the right-hand side XPM sideband as a function of the frequency spacing detuning between λ_1 and λ_2 . A second-order polynomial function is used for curve fitting. The 3 dB bandwidth of the AORFSA is measured to be 1.69 THz for the TM mode of the proposed slot and only 0.41 THz for the TE mode of the conventional channel waveguide with the same length of 50 cm. In the experiment, we chose the TM mode for the slot-waveguide and the TE mode for the channel waveguide since they have a larger bandwidth than their counter-polarization modes. The proposed slot-waveguide shows an over-three-fold enhancement in its 3 dB measurement bandwidth, which mainly benefits the reduced dispersion parameter for easing the group velocity “walk-off” issue over the operation band. According to (8), using all the parameters in the experiment, the calculated ideal 3 dB bandwidth of the AORFSA for the TM mode of the slot-waveguide is estimated to be 8.75 THz. This value is much larger than the actually measured bandwidth of 1.69 THz since experimental disturbances such as unwanted FWMs and residual ASE noise exist [16]. This may also imply that the real bandwidth of the AORFSA harnessing

the proposed slot-waveguide can be potentially larger than the measured value of 1.69 THz, which makes it suitable for terahertz measurement applications.

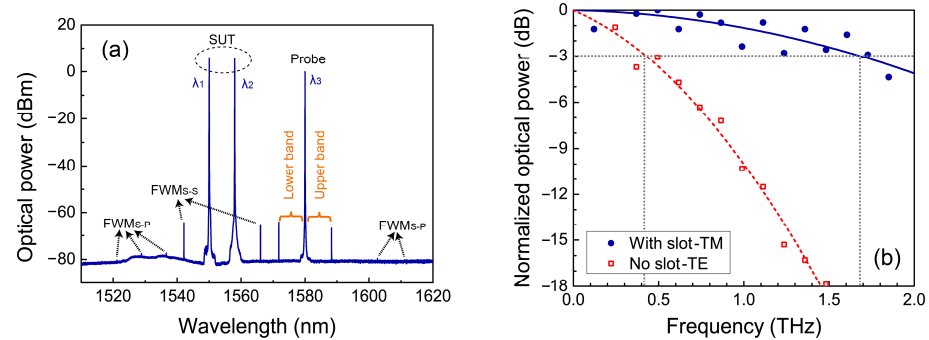


Figure 4. (a) The optical spectrum of the AORFSA bandwidth measurement. (b) Normalized XPM power as a function of the frequency spacing of the two wavelengths of the SUT.

4.2. Sensitivity

The sensitivity of the AORFSA refers to the lowest input power of the SUT that can be detected. It can be defined as the input SUT power that makes the generated XPM signal 3 dB higher than the noise level of the OSA. Besides the noise level of the OSA, the AORFSA sensitivity is also determined by the input power of the probe beam, the propagation length and the nonlinearity coefficient γ of the used waveguide. Considering the linear loss coefficient α , the propagation length is modified with an effective propagation length $L_{\text{eff}} = [1 - \exp(-\alpha L)]/\alpha$. To measure the sensitivity, λ_1 , λ_2 and λ_3 are fixed at 1550 nm, 1555 nm and 1580 nm, respectively. Focusing on the measuring signal with a frequency of 625 GHz (i.e., 5 nm between λ_1 and λ_2), we fix the probe power to 7 dBm and vary the SUT input power to the waveguide from 2 dBm to 14 dBm, then measure the corresponding power of the generated XPM signal. The result of the output XPM power as a function of the input SUT power is shown in Figure 5a. Good linear fitting is observed, which shows that its dynamic range is larger than 25 dB. Due to the limited input power of the lasers in our experiments, the actual dynamic range may be even larger. The sensitivity in this scenario is observed to be 3 dBm, and the corresponding optical spectrum is shown in Figure 5b. This sensitivity measurement is also affected by the wavelength spacing between the probe and SUT and/or the focused measuring frequency. By decreasing this wavelength spacing and/or measuring frequency, the group velocity “walk-off” effect can be mitigated, which may increase the SNR of the XPM process and the sensitivity of the AORFSA.

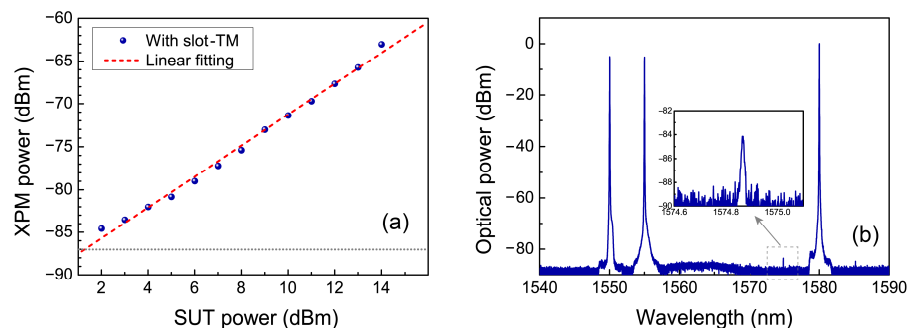


Figure 5. (a) The XPM sideband power as a function of the averaged input SUT power with the testing frequency fixed at 625 GHz. (b) The corresponding optical spectrum when the generated XPM sideband is about 3 dB higher than the noise level of the OSA.

The proposed slot-waveguide is designed with smaller dispersion and a comparable nonlinearity coefficient compared with the standard structure, which indicates that we could use a longer waveguide to enlarge the accumulated nonlinearity for increasing the

SNR and sensitivity if we focus on the same measuring bandwidth. For example, supposing we need to obtain the same bandwidth with the TM mode, given the same parameters as in the experiment above, i.e., $\lambda_1 = 1550$ nm, $\lambda_2 = 1555$ nm and $\lambda_3 = 1580$ nm for both the slot and channel waveguides, the length we could use for the slot-waveguide is 8.44 times as long as that for the channel waveguide, according to (8). Thus, with the same input power of the probe and SUT, the output power of the generated XPM signal could be 19 dB higher for the AORFSA with the slot-waveguide. Given the same noise level as the OSA, the AORFSA's sensitivity can be increased by at least 10 dB with the longer slot-waveguide.

4.3. Wavelength-Dependence

The dispersion of the proposed slot-waveguide is carefully engineered so that the AORFSA based on it can work over the whole C and L bands. However, the dispersion parameter varies slowly with the operation wavelength, which will affect the 3 dB bandwidth of the AORFSA due to the different degree of group velocity mismatch. To measure this property, we repeat the bandwidth measurement experiment as discussed above, changing the probe wavelength λ_3 to 1580 nm, 1575 nm and 1565 nm, respectively. For each group of measurements, the measuring frequency of the SUT (i.e., the frequency spacing between λ_1 and λ_2) is detuned from 0 to 1.9 THz, and the wavelength spacing between the probe and the SUT remains the same at about 20 nm. Figure 6a shows the results of the three groups of bandwidth measurement experiments. The 3 dB bandwidth is measured to be 1.69 THz, 1.02 THz and 0.72 THz when the probe beam is fixed at 1580 nm, 1575 nm and 1565 nm, respectively. We can observe that, as the operation wavelength decreases, the 3 dB bandwidth also decreases due to the increased dispersion at a shorter wavelength. The simulated bandwidth of the AORFSA as a function of probe wavelength is shown in Figure 6c. The relationship between the dispersion variation and the corresponding 3 dB bandwidth fits well with the trend of (8), though the measuring bandwidth is actually smaller than its calculated value. Accordingly, the 3 dB bandwidth of the AORFSA based on our 50 cm long slot-waveguide could be larger if we moved the wavelength of the SUT to around 1580 nm, but we cannot really measure it due to equipment limitations. Nevertheless, the probe signal λ_3 was fixed at 1580 nm in other sections of this paper, far away from the SUT signals, to avoid the detrimental spectral overlap between the FWM signals and the necessary measurement band of the probe [8,11].

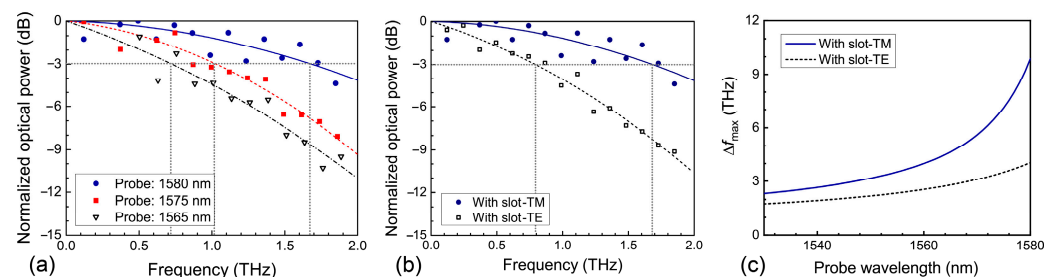


Figure 6. Normalized XPM power as a function of the frequency spacing of the two wavelengths of the SUT for (a) different probe and SUT wavelength locations, and (b) both the TM and TE modes of the slot-waveguide. (c) The simulated bandwidth of the AORFSA as a function of probe wavelength.

4.4. Polarization-Dependence

In some applications, we can utilize the two orthogonal polarizations as the two channels in the AORFSA [13]. Here, we investigate the polarization property of the AORFSA based on the proposed slot-waveguide. With the same experimental setup and parameters, the bandwidth of the AORFSA for the TE mode of the slot-waveguide is also measured. Figure 6b shows the bandwidth measurement results of both the TE and TM modes. Compared with the TM mode, the 3 dB bandwidth of the AORFSA with the TE mode is reduced to 0.8 THz due to the increased dispersion. If the same bandwidth of the

two modes is required, the operating wavelengths of both the probe beam and the SUT should be carefully chosen, which, however, is not necessary in most cases.

5. Conclusions

In summary, the performances of the AORFSA built on CMOS-compatible optical waveguides with and without the slot are investigated and compared. Besides its low linear and negligible nonlinear losses, the high-index doped silica glass slot-waveguide has a smaller dispersion parameter and slightly larger nonlinearity in the C and L bands for the AORFSA applications. Compared with the conventional channel waveguide with an equal length of 50 cm, the measured 3 dB bandwidth of the AORFSA of the slot-waveguide at 1.69 THz is approximately three times that of a waveguide with the same geometry but with the slot removed. We also investigated the sensitivity between these waveguides and found that the SNR and sensitivity could increase by 19 dB and 10 dB, respectively, with a longer slot-waveguide. We believe that our proposed CMOS-compatible slot-waveguide further optimizes the properties of the AORFSA and can find extensive applications in signal spectrum analysis with terahertz bandwidth.

Author Contributions: Conceptualization, K.Z., Y.L. and S.-T.C.; methodology, Y.L. and Z.K.; software, Y.L. and W.-L.H.; validation, Z.K., B.E.L. and S.-T.C.; formal analysis, Y.L.; investigation, Y.L. and Z.K.; resources, W.-L.H., R.R.D. and B.E.L.; data curation, Y.L., Z.K. and S.-T.C.; writing—original draft preparation, Y.L.; writing—review and editing, K.Z., Z.K., B.E.L. and S.-T.C.; visualization, Y.L. and Z.K.; supervision, S.-T.C. and K.Z.; project administration, K.Z.; funding acquisition, Y.L. and Z.K. All authors have read and agreed to the published version of the manuscript.

Funding: This research was funded by the National Natural Science Foundation of China (Nos. 62105291 and 62075188), the Zhejiang Provincial Natural Science Foundation of China (No. LY21F050007), the Science Foundation of Zhejiang Sci-Tech University (No. 11430131282104) and the Open Fund of IPOC (BUPT) (No. IPOC2022A01).

Data Availability Statement: Data are contained within the article.

Conflicts of Interest: The authors declare no conflict of interest.

References

1. Weber, H.-G.; Ludwig, R. Ultra-high-speed OTDM transmission technology. In *Optical Fiber Telecommunications VB*; Elsevier: New York, NY, USA, 2008; pp. 201–232.
2. Vo, T.D.; Pelusi, M.D.; Schroder, J.; Corcoran, B.; Eggleton, B.J. Multi-impairment monitoring at 320 Gb/s based on cross-phase modulation radio-frequency spectrum analyzer. *IEEE Photonics Technol. Lett.* **2010**, *22*, 428–430. [[CrossRef](#)]
3. Vo, T.; Pelusi, M.; Schroeder, J.; Luan, F.; Madden, S.; Choi, D.-Y.; Bulla, D.; Luther-Davies, B.; Eggleton, B. Simultaneous multi-impairment monitoring of 640 Gb/s signals using photonic chip based RF spectrum analyzer. *Opt. Express* **2010**, *18*, 3938–3945. [[CrossRef](#)] [[PubMed](#)]
4. Walmsley, I.A.; Dorrer, C. Characterization of ultrashort electromagnetic pulses. *Adv. Opt. Photonics* **2009**, *1*, 308–437. [[CrossRef](#)]
5. Von der Linde, D. Characterization of the noise in continuously operating mode-locked lasers. *Appl. Phys. B* **1986**, *39*, 201–217. [[CrossRef](#)]
6. Capmany, J.; Novak, D. Microwave photonics combines two worlds. *Nat. Photonics* **2007**, *1*, 319. [[CrossRef](#)]
7. Ou, H.; Ye, C.; Zhu, K.; Hu, Y.; Fu, H. Millimeter-wave harmonic signal generation and distribution using a tunable single-resonance microwave photonic filter. *J. Lightwave Technol.* **2010**, *28*, 2337–2342.
8. Pelusi, M.; Luan, F.; Vo, T.D.; Lamont, M.R.; Madden, S.J.; Bulla, D.A.; Choi, D.-Y.; Luther-Davies, B.; Eggleton, B.J. Photonic-chip-based radio-frequency spectrum analyser with terahertz bandwidth. *Nat. Photonics* **2009**, *3*, 139–143. [[CrossRef](#)]
9. Eggleton, B.J.; Vo, T.D.; Pant, R.; Schr, J.; Pelusi, M.D.; Yong Choi, D.; Madden, S.J.; Luther-Davies, B. Photonic chip based ultrafast optical processing based on high nonlinearity dispersion engineered chalcogenide waveguides. *Laser Photonics Rev.* **2012**, *6*, 97–114. [[CrossRef](#)]
10. Chen, L.; Duan, Y.; Zhou, H.; Zhou, X.; Zhang, C.; Zhang, X. Real-time broadband radio frequency spectrum analyzer based on parametric spectro-temporal analyzer (PASTA). *Opt. Express* **2017**, *25*, 9416–9425. [[CrossRef](#)]
11. Dorrer, C.; Maywar, D. RF spectrum analysis of optical signals using nonlinear optics. *J. Lightwave Technol.* **2004**, *22*, 266. [[CrossRef](#)]
12. Corcoran, B.; Vo, T.D.; Pelusi, M.D.; Monat, C.; Xu, D.-X.; Densmore, A.; Ma, R.; Janz, S.; Moss, D.J.; Eggleton, B.J. Silicon nanowire based radio-frequency spectrum analyzer. *Opt. Express* **2010**, *18*, 20190–20200. [[CrossRef](#)] [[PubMed](#)]
13. Ma, M.; Adams, R.; Chen, L.R. Integrated photonic chip enabled simultaneous multichannel wideband radio frequency spectrum analyzer. *J. Light. Technol.* **2017**, *35*, 2622–2628. [[CrossRef](#)]

14. Vo, T.D.; Corcoran, B.; Schroder, J.; Pelusi, M.D.; Xu, D.-X.; Densmore, A.; Ma, R.; Janz, S.; Moss, D.J.; Eggleton, B.J. Silicon-chip-based real-time dispersion monitoring for 640 Gbit/s DPSK signals. *J. Lightwave Technol.* **2011**, *29*, 1790–1796. [[CrossRef](#)]
15. Pelusi, M.; Vo, T.D.; Luan, F.; Madden, S.J.; Choi, D.-Y.; Bulla, D.; Luther-Davies, B.; Eggleton, B.J. Terahertz bandwidth RF spectrum analysis of femtosecond pulses using a chalcogenide chip. *Opt. Express* **2009**, *17*, 9314–9322. [[CrossRef](#)] [[PubMed](#)]
16. Ferrera, M.; Reimer, C.; Pasquazi, A.; Peccianti, M.; Clerici, M.; Caspani, L.; Chu, S.T.; Little, B.E.; Morandotti, R.; Moss, D.J. CMOS compatible integrated all-optical radio frequency spectrum analyzer. *Opt. Express* **2014**, *22*, 21488–21498. [[CrossRef](#)] [[PubMed](#)]
17. Li, Y.; Kang, Z.; Zhu, K.; Ai, S.; Wang, X.; Davidson, R.R.; Wu, Y.; Morandotti, R.; Little, B.E.; Moss, D.J.; et al. All-optical RF spectrum analyzer with a 5 THz bandwidth based on CMOS-compatible high-index doped silica waveguides. *Opt. Lett.* **2021**, *46*, 1574–1577. [[CrossRef](#)] [[PubMed](#)]
18. Dizaji, M.R.; Krüchel, C.J.; Fülöp, A.; Andrekson, P.A.; Chen, L.R. Silicon-rich nitride waveguides for ultra-broadband nonlinear signal processing. *Opt. Express* **2017**, *25*, 12100–12108. [[CrossRef](#)]
19. Liu, Q.; Gao, S.; Li, Z.; Xie, Y.; He, S. Dispersion engineering of a silicon-nanocrystal-based slot waveguide for broadband wavelength conversion. *Appl. Opt.* **2011**, *50*, 1260–1265. [[CrossRef](#)]
20. Mas, S.; Caraquitena, J.; Galán, J.V.; Sanchis, P.; Martí, J. Tailoring the dispersion behavior of silicon nanophotonic slot waveguides. *Opt. Express* **2010**, *18*, 20839–20844. [[CrossRef](#)]
21. Zhang, L.; Yan, Y.; Yue, Y.; Lin, Q.; Painter, O.; Beausoleil, R.G.; Willner, A.E. On-chip two-octave supercontinuum generation by enhancing self-steepening of optical pulses. *Opt. Express* **2011**, *19*, 11584–11590. [[CrossRef](#)]
22. Zhu, M.; Liu, H.; Li, X.; Huang, N.; Sun, Q.; Wen, J.; Wang, Z. Ultrabroadband flat dispersion tailoring of dual-slot silicon waveguides. *Opt. Express* **2012**, *20*, 15899–15907. [[CrossRef](#)] [[PubMed](#)]
23. Boggio, J.C.; Bodenmüller, D.; Fremberg, T.; Haynes, R.; Roth, M.; Eisermann, R.; Lisker, M.; Zimmermann, L.; Böhm, M. Dispersion engineered silicon nitride waveguides by geometrical and refractive-index optimization. *JOSA B* **2014**, *31*, 2846–2857. [[CrossRef](#)]
24. Zhang, L.; Yue, Y.; Xiao-Li, Y.; Beausoleil, R.G.; Willner, A.E. Highly dispersive slot waveguides. *Opt. Express* **2009**, *17*, 7095–7101. [[CrossRef](#)]
25. Li, Y.; Li, J.; Huo, Y.; Chen, M.; Yang, S.; Chen, H. Spatial-mode-coupling-based dispersion engineering for integrated optical waveguide. *Opt. Express* **2018**, *26*, 2807–2816. [[CrossRef](#)]
26. Moss, D.J.; Morandotti, R.; Gaeta, A.L.; Lipson, M. New CMOS-compatible platforms based on silicon nitride and Hydex for nonlinear optics. *Nat. Photonics* **2013**, *7*, 597–607. [[CrossRef](#)]
27. Ferrera, M.; Razzari, L.; Duchesne, D.; Morandotti, R.; Yang, Z.; Liscidini, M.; Sipe, J.; Chu, S.; Little, B.E.; Moss, D.J. Low-power continuous-wave nonlinear optics in doped silica glass integrated waveguide structures. *Nat. Photonics* **2008**, *2*, 737–740. [[CrossRef](#)]
28. Xu, Q.; Almeida, V.R.; Panepucci, R.R.; Lipson, M. Experimental demonstration of guiding and confining light in nanometer-size low-refractive-index material. *Opt. Lett.* **2004**, *29*, 1626–1628. [[CrossRef](#)]
29. Xiao-Li, Y. Light guiding in a slot waveguide that includes an additional confining core region. *Opt. Express* **2010**, *18*, 6408–6416. [[CrossRef](#)]
30. Vallaitis, T.; Bogatscher, S.; Alloatti, L.; Dumon, P.; Baets, R.; Scimeca, M.L.; Biaggio, I.; Diederich, F.; Koos, C.; Freude, W. Optical properties of highly nonlinear silicon-organic hybrid (SOH) waveguide geometries. *Opt. Express* **2009**, *17*, 17357–17368. [[CrossRef](#)]

Disclaimer/Publisher’s Note: The statements, opinions and data contained in all publications are solely those of the individual author(s) and contributor(s) and not of MDPI and/or the editor(s). MDPI and/or the editor(s) disclaim responsibility for any injury to people or property resulting from any ideas, methods, instructions or products referred to in the content.